Enhanced dispersion of prussian blue via intercalation into layered double hydroxides for efficient solar seawater evaporation

Weixin Mo, Qianqian Hu, Jun Guan, Yu Jiang, Weiliang Tian, Huiyu Li, Fabrice Leroux, Yongjun Feng

Enhanced Dispersion of Prussian Blue via Intercalation into Layered Double Hydroxides for Efficient Solar Seawater Evaporation

Weixin Mo[a], Qianqian Hu[a], Jun Guan[a], Yu Jiang[b], Weiliang Tian[c], Huiyu Li[a,*], Fabrice Leroux[d], Yongjun Feng [a,c,*]

[a.] *State Key Laboratory of Chemical Resource Engineering, College of Chemistry, Beijing University of Chemical Technology, No. 15 Beisanhuan East Road, Beijing, 100029, China.*

[b.] *Beijing Municipal Construction Group Co. Ltd, A40 Xingshikou Road, Haidian District, Beijing, China, 100195.*

[c.] *College of Chemistry and Chemical Engineering, Tarim University, Alar, 843300, PR China*

[d.] *Chemical Institute of Clermont-Ferrand (ICCF), University Clermont Auvergne, UMR-CNRS No 6296, F_63171 Aubière, France*

Prussian blue (PB) is favored for its photothermal absorption capability in solar vapor generation applications. However, the photothermal conversion efficiency of current PB-based devices is limited by the material's poor dispersion. Herein, we report a method of incorporating PB in the interlayers of layered double hydroxides (LDHs) to prevent its aggregation. The dispersion is further enhanced and stabilized by the addition of sodium dodecyl sulfate (SDS). The thermal and water stability of PB is improved due to the rigid structure of LDHs and interactions between layers and anions. Elemental analysis confirms that with the increase of molar ratio of Mg/Al and the introduction of SDS, concentrations of PB are decreased accordingly. As a result, the rate of solar vapor generation is increased by 35.9% for powders containing 50 mg of equivalent PB. Of note, converting this material into a three-dimensional structure of high rebound foam further enhances solar water evaporation rate, from 0.79 $kg \cdot m^{-2} \cdot h^{-1}$ to 0.98 $kg \cdot m^{-2} \cdot h^{-1}$, with only 20 mg of equivalent PB, increasing the corresponding photothermal conversion efficiency from 53.8% to 66.3%.

Introduction

Freshwater is fundamental to the sustenance and advancement of civilizations, yet less than 0.36% of the Earth's total water resources can be directly used by mankind. Due to the compounding challenges of climate change, population growth, and rampant pollution, more than two-thirds of the population around the world has been facing varying degrees of water scarcity. [1-4] Advanced technologies such as reverse osmosis membrane technology,[5] electrodialysis[6] and multi-stage flash distillation technology[7] have been developed to resolve the global crisis through seawater desalination. However, these technologies are often hampered by their high energy consumption and the requirement of well-developed infrastructure and centralized installations,[8] restricting their applicability in remote areas. Conversely, solar distillation presents a low-energy alternative for providing clean water.

In the development of solar distillation, the photothermal agent plays a key role in its efficiency. Prussian blue (PB) and its analogs (PBAs) possess a stable face-centered cubic structure consisting of ferric, ferrous, and cyanide ions with a F_{m3m} space group.[9, 10] PB has shown applications in diverse areas including batteries,[11] catalysis,[12] biosensors,[13] energy storage,[14] removal of cesium,[15] and biofriendly magnetic resonance imaging,[16] thanks to their magnetic, electrochemical, and biocompatible properties.[17] Owing to its efficient light absorption properties compared with metal nanoparticles and carbon dots, PB emerges as a promising photothermal agent for solar energy conversion.[18] However, the tendency to aggregate [19] adversely limits its photothermal efficiency. Recent studies have sought to solve this by dispersing PB within other host materials. For example, Fang et al. [20] loaded PB nanocrystals on cotton fiber and synthesized photothermal composite materials to purify organic solvents. The dispersed PB molecules showed a high photothermal interfacial evaporation rate in polar organic solvents. Wang et al. [21] used phytic acid-doped polypyrrole for controllable growth of PB on cotton fibers. However, the developed photothermal agents are not suitable for applications in aqueous environments, which is a key aspect in solar distillation, since water can leach out PB crystals and more organic materials can pollute the environment. The dispersed and stabilized PB materials exhibiting excellent photothermal properties are desirable in the solid state for water evaporation.

To address these limitations, two-dimensional (2D) layered double hydroxides (LDHs) as host structures can protect and disperse PB.[22-24] LDHs consist of positively charged metallic layers, interlayer anions, and water, i.e., $[M^{2+}_{1-x}M^{3+}_{x}(OH)_2]^{x+}A^{n-}_{x/n}\cdot yH_2O$, which makes them suitable for applications in aqueous environments. M^{2+} and M^{3+} are divalent and trivalent metals ions, respectively, and A^{n-} represents an n-valent anion.[25, 26] LDHs provide highly tunable chemical composition (both cations in the hydroxide layers and the interlayer anions) with relatively easy synthesis. Various anions including organic and inorganic anions, coordination compounds, polyoxometalates and biomolecules can be intercalated.[26] Besides, different molar ratios of M^{2+}/M^{3+} can change the concentration and the dispersion of anions in the interlayer.[27] The rigid layers build a stable and protective structure, and limited molecules can be confined in the interlayer, which prevents the molecules from moving and piling up. LDHs host structure is an ideal platform to disperse PB in the solid state and improve the photothermal efficiency of PB.[28] However, few literatures have modified the structure of LDHs with a special attention to controllably increase the dispersion of PB.

In this work, we have developed an efficient and stable photothermal agent for solar evaporation by intercalating of PBA into MgAl-LDHs through a co-precipitation method. The highest dispersion of PBA is obtained by finely optimized the molar ratio between divalent and trivalent metals (labeled as PBA@LDHs). Furthermore, long alkyl chain surfactant, sodium dodecyl sulfate (SDS), is co-intercalated into LDHs together with PBA and then the SDS species prevent from the aggregation of PB in the interlayer region (marked as SDS-PBA@LDHs).[29-31] The structural and photophysical properties of different series LDHs are analyzed using various techniques. In the range of pH value from 7 to 10, specifically, LDHs exhibited excellent stability towards water. The obtained powders are transformed into foam, which is investigated for photothermal-water evaporation performance.

Experimental

Chemicals

All reagents were purchased from commercial suppliers and used without further purification. Magnesium nitrate hexahydrate ($Mg(NO_3)_2\cdot6H_2O$, 99.5%) and ferrous chloride ($FeCl_2\cdot4H_2O$, 99%) were bought from Sinopharm Chemical Reagent Co., Ltd. Aluminum nitrate nonahydrate ($Al(NO_3)_3\cdot9H_2O$, 99%), sodium hydroxide (NaOH, 95%), Sodium bicarbonate ($NaHCO_3$, 99.5%) and sodium dodecyl sulfate ($CH_3(CH_2)_{11}SO_4Na$, 92.5-100.5%) were purchased from Shanghai Macklin Biochemical Co., Ltd. Potassium ferricyanide ($K_3[Fe(CN)_6]$, 99.5%) was obtained from Beijing Tong Guang Fine Chemicals Co. Additionally, the high rebound compounds A (Polyether) and B (Isocyanate) were supplied by Liming Research Institute of Chemical Industry.

Synthesis of PBA@LDHs

A co-precipitation method as per literature[32, 33] was utilized to synthesize PBA@LDHs with different molar ratios of magnesium to aluminum. The obtained samples were labeled as PBA@LDHs-x, where x presents the molar ratio of Mg/Al, x=2,3,4. Take the synthesis of PBA@LDHs-2 (scheme 1a) for example: 0.024 mol of $Mg(NO_3)_2\cdot6H_2O$ and 0.012 mol of $Al(NO_3)_3\cdot9H_2O$ were dissolved in 100 mL of deionized water to prepare solution A. 0.072 mol of NaOH was dissolved in 100 mL of deionized water as solution B, and solution C was 100 mL aqueous solution of $K_3[Fe(CN)_6]$ ($n(K_3[Fe(CN)_6])=n(Al(NO_3)_3)$). Solution A was added dropwise into solution C at a rate of 5

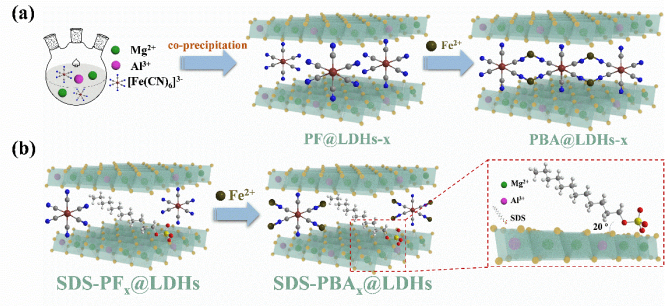

Scheme. 1 The schematic diagram for the syntheses of (a)PBA@LDHs-x and (b)SDS-PBA$_x$@LDHs.

mL/min under constant stirring and N_2 atmosphere, and solution B was added to maintain a pH of 9.5. Thereafter, the mixture was aged for 11 h with continuous stirring at 80°C under N_2. The solid was collected through centrifugation of the as-prepared mixture and washed with deionized water to remove any residual reactants. The obtained product (labeled as PF@LDHs-x, where PF denotes Potassium ferricyanide) was then mixed with a specified amount of $FeCl_2\cdot4H_2O$ and magnetically stirred for 4 h. The resultant products were collected, washed with methanol, and freeze-dried overnight. The procedures for PBA@LDHs-3 and PBA@LDHs-4 followed similar synthesis procedure but with higher ratios of Mg to Al.

Preparation of SDS-PBA$_x$@LDHs

SDS-PBA$_x$@LDHs were synthesized through co-precipitation procedure as shown in scheme 1b. 0.024 mol of $Mg(NO_3)_2{\cdot}6H_2O$ with 0.006 mol of $Al(NO_3)_3{\cdot}9H_2O$ were added in 100 mL of deionized water (the molar ratio of Mg to Al is 4). The as-prepared solution was added dropwise into a 100 mL aqueous solution of SDS (a mol) and $K_3[Fe(CN)_6]$ (b mol). An NaOH aqueous solution was utilized to maintain the pH at 9.5. The x value refers to the feeding molar ratio of $K_3[Fe(CN)_6]$/SDS, calculated as x (%) = b/a × 100 (%) and a + 3b = n(Al^{3+}). Thereafter, the mixture was aged for 11 h under stirring at 80°C and N_2 atmosphere. The obtained product (labeled as SDS-PF$_x$@LDHs) was mixed with $FeCl_2{\cdot}4H_2O$ and stirred for 4 h at room temperature.

Preparation of PBA@LDHs/PU

To synthesize PBA@LDHs/PU, high rebound compound B was mixed with PBA@LDHs-x or SDS-PBA$_x$@LDHs powder containing 20 mg of an equivalent amount of PB. The mixture was added with high rebound compound A and stirred intensely until bubbles formed. The obtained foam was cut to uniform size.

Characterization

The phase analysis of PBA@LDHs-x and SDS-PBA$_x$@LDHs was carried out using powder X-ray diffraction (XRD) technique. The X-ray diffractometer (Philips X'Pert Pro) with Cu Kα radiation (λ = 1.5406 Å) was employed, over a 2θ range from 3 to 80° with a scanning step of 10° min^{-1}. The chemical analysis of sample was carried out using Fourier transform infrared spectroscopy with a resolution of 4 cm^{-1} (Thermo-Nicolet 5700 FT-IR spectrometer equipped with transmission mode). The samples were investigated at room temperature in 4000-400 cm^{-1} using the KBr pellet technique. UV-Vis-NIR absorption spectroscopy was performed by a Shimadzu UV-3600 spectrophotometer equipped with an integrating sphere in the range of 220-2500 nm. The concentration of C, H, N, and S was obtained by Elemental analyzer system (Vairo EL CUBE-CHNS mode). The morphology and crystal structure analysis were carried out using scanning electron microscopy (ZEISS Supra 55) and transmission electron microscopy (FEI Talos F200x). Thermal stability was measured by a HTIACHI STA7300 instrument. The concentration of Fe was obtained by Agilent ICP-OES 5800.

Solar water evaporation performance measurement

Solar water evaporation performance was measured in two scenarios: powder and foam. For the powder scenario (Scheme 2a), the simulated solar irradiation was provided by a solar simulator (AT1 Pro, Ledesk) with a light density of 1 $kW{\cdot}m^{-2}$. A commercial polyurethane foam was placed inside a glass container (opening diameter of 10 cm) containing 70 mL of seawater (Bohai Sea, China). The powder sample was placed on the top of foam, and the simulated sunlight was irradiated vertically from the top onto the material. The glass container was placed on an electronic analytical balance to monitor changes in mass every 5 min. For the foam scenario (Scheme 2b), the container was covered with aluminum foil, which had a hole the same size as the foam sample (diameter of 47 mm). The samples were floatable, allowing direct irradiation by the simulated sunlight. The surface temperature of the samples was measured by an infrared camera. All test data were collected at an ambient temperature of 22 - 23°C and a relative humidity of 26 ± 5%. The evaporation performance is calculated in term of the solar-vapor efficiency (η) via equation 1:[34-36]

$$\eta = \dot{m}h_V/C_{opt}P_0 \qquad (1)$$

where $\dot{m}$ represents mass flux, h_V represents latent heat of vaporization for water (2.44 $MJ{\cdot}kg^{-1}$). C_{opt} measures the optical concentration on the absorber surface, and P_0 refers to the solar irradiation power of 1 sun (1 $kW{\cdot}m^{-2}$).

Results and discussion

Structure analysis of LDHs

Fig. 1a-b shows the powder XRD patterns of PF@LDHs, PBA@LDHs, and SDS-PBA@LDHs. All the XRD patterns demonstrate characteristic peaks of layered double

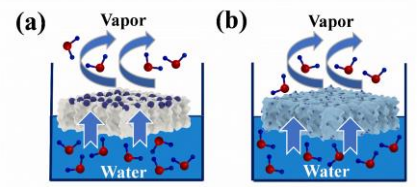

Scheme. 2 The schematic diagram of water evaporation device in (a) powder and (b) foam scenarios.

hydroxides.[37, 38] For all the samples, the basal spacing of $d_{(003)}$ = 1.07 nm indicates that $[Fe(CN)_6]^{3-}$ anion is situated in the interlayer of LDHs.[39] Besides, the incorporation of Fe^{2+} shows no shift in the (00*l*) plane, indicating no influence on the distance between the cationic layers of LDH structure. The diffraction peaks of (003) of SDS-PF$_x$@LDHs and SDS-PBA$_x$@LDHs show the basal spacing of

$d_{(003)}$ = 1.07 nm, while a basal length of 1.78 nm is measured in SDS molecules. It is conferred that the basal *d*-spacing of co-intercalated LDHs is imposed by the Prussian blue between the layers, rather than by SDS molecules, owing to the proportions of interlayered anions.[40] The thickness of the metal hydroxide layers is 0.48 nm, leading to 20° tilt angle of the interlayer surfactant.[41, 42] Moreover, the (110) reflection for all the samples confirms the integrity of the hydroxide sheets of LDHs.

The FTIR spectra disclose the structural properties of as-prepared LDHs nanoparticles (Fig. 1c-d). LDHs samples demonstrate the characteristic adsorption peaks of hydrotalcite at 423 cm^{-1}, ascribed to the stretching vibration of Mg-O and Al-O. A broad band around 3400 cm^{-1} is observed, which is attributed to the OH stretching vibration of the octahedral layer and intercalated water molecules.[43] The sharp bands at 2040 cm^{-1} and 2110 cm^{-1} correspond to the stretching mode of the CN group in hexacyanoferrate species. These two peaks correspond to hexacyanoferrate (II) and hexacyanoferrate (III), respectively. This phenomenon indicates that a part of Fe(III) is reduced to Fe(II) during intercalation,[44, 45] which deviates from the peak observed at 2086 cm^{-1} (Fe(II)-CN stretching vibrations) for Prussian blue. The S=O antisymmetric stretches appear at 1222 cm^{-1}, verifying SDS intercalated LDHs. The peaks located at 2925 cm^{-1} and 2850 cm^{-1} are ascribed to the antisymmetric and symmetric stretching modes of -CH, respectively.[46]

Microstructure analysis

Fig. 2 displays the morphologies of prepared LDHs. LDHs platelets exhibit a flower-like structure (Fig. $2a_1$-e_1), resulting in the aggregation of LDHs sheets into a flaky shape (Fig. $2a_2$-e_2).

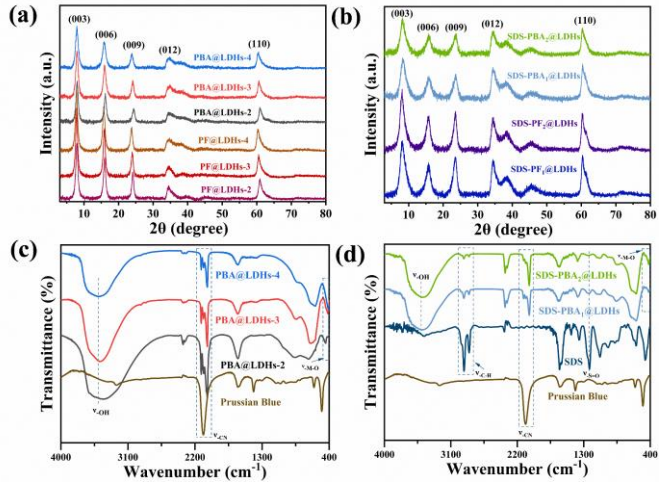

Fig. 1 Powder XRD spectra (a, b) and FT-IR spectra (c, d) of PBA@LDHs, SDS-PBA@LDHs, Prussian blue, and SDS.

LDHs sheets successfully retain their inherent structure. Moreover, the distribution of Al and Fe elements is depicted in Fig. $2a_3$-e_4, with both elements demonstrating a uniform distribution. The distribution of Fe corresponds to the position of Al, indicating PB is dispersed in the gallery of LDHs. On other hand, Prussian blue occupies limited space within the galleries, impeding 3D aggregation.

Fig. S1 (Supporting information) shows the morphologies of SDS-PBA_2@LDHs/PU. The foam composite material has pores tens to hundreds of microns in diameter, allowing water to be efficiently transported. In addition, the powder sample is successfully dispersed on the foam (Fig. S1b), demonstrating good compatibility between LDHs and the foam.

Light absorption property analysis

Solid UV-Vis-NIR spectroscopy is used to measure the light-absorbing properties of LDHs. In Fig. 3a, the light absorption of powder diminishes with an increase in the molar ratio of Mg/Al, which corresponds to a decreased concentration of PB in LDHs.

The co-intercalation of SDS further disperses the PB molecules within the interlayer spaces, resulting in reduced concentrations of PB and weaker light absorption. Furthermore, Fig. 3b demonstrates the transmission, reflection, and absorption spectra of LDHs foams. The absorption, *A*, can be calculated according to equation 2:

$$A = 1 - R - T \quad (2)$$

where *A*(%), *R*(%), and *T*(%) refer to absorption, reflection, and transmission, respectively.[47] As the dispersion of PB is increased, namely from PB to SDS-PBA_2@LDHs, the light absorption enhances from 55% to 71%. However, an overly extensive dispersion of PB reduces the absorption rate. The aggregation of PB molecules impedes photothermal conversion due to the light being shielded by the surface molecules. Optimal separation allows light to engage more surface area. However, if the molecules are excessively dispersed, the transfer of electron between molecules is impeded, leading to the reduced

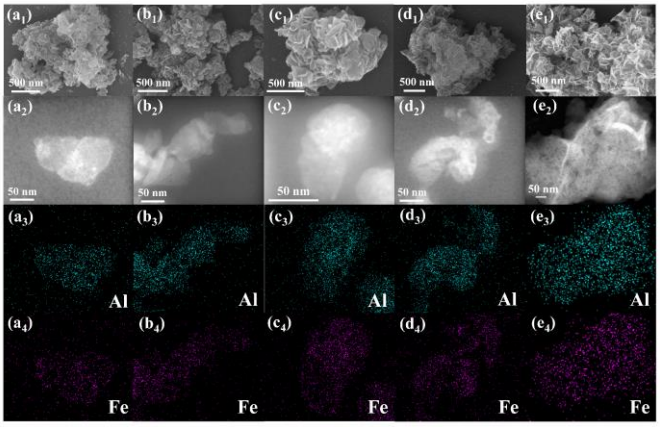

Fig. 2 Morphologies of (a) PBA@LDHs-2, (b) PBA@LDHs-3, (c) PBA@LDHs-4, (d)SDS-PBA_2@LDHs and (e) SDS-PBA_1@LDHs; (a_1-e_1) SEM images, (a_2-e_2) TEM images, and (a_3-e_4) EDS elemental mapping.

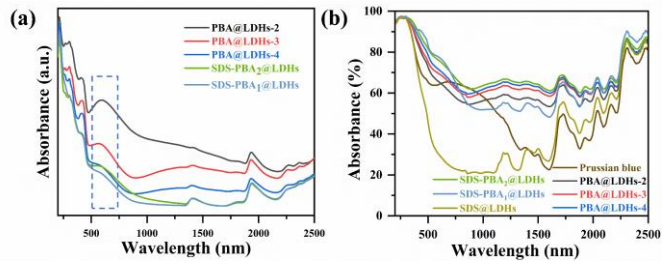

Fig. 3 UV-Vis-NIR spectra of PBA@LDHs and SDS-PBA@LDHs: (a) powder and (b) foams.

light absorption. All samples show similar absorption profile within 1500-2500 nm wavelength range, and reveal that PB possesses low absorption in the near-infrared region. Notably, SDS-LDHs combined with high rebound compounds demonstrate the lowest light absorption. Therefore, SDS and LDHs act as dispersants and do not contribute significantly to absorption.

Structural stability analysis

Fig. 4 depicts TG-DTA analysis of the thermal stability of PB and LDHs. The thermal degradation of PB occurs in three distinct steps. The first mass loss accounts for the water evaporation below 180°C, the second step is ascribed to the gradual loss of CN from 180 to 270°C, and the final loss corresponds to the decomposition of the material into iron oxide beyond 270°C.[48] The DTA profile indicates that the decomposition of PB to iron oxide is exothermic with heat release. In the case of LDHs, a similar triphasic mass loss pattern is observed. From TG curves, the mass loss below 170°C results from the removal of adsorbed water, the dehydroxylation takes place during the temperature

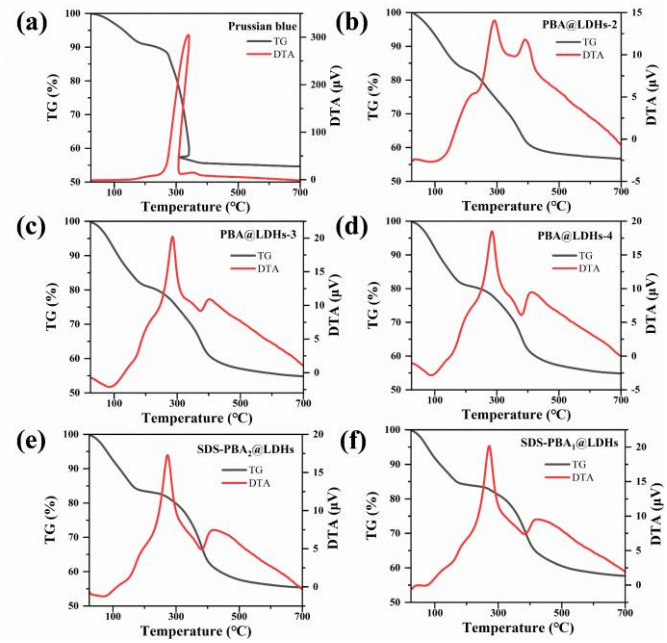

Fig. 4 TG-DTA curves of PB and corresponding LDHs at 10°C/min.

ranging from 170 to 310°C, with a prominent loss occurred at 270°C. The final phase of mass reduction is due to the continued dehydroxylation and decomposition of both PB and dodecyl sulfate over 310°C.[49] It is noted that the intercalation improves the thermal stability of PB due to the van der Waals force and electrostatic interactions between intercalated anions and LDHs layers.[50, 51]

Solar vapor generation analysis

The effect of LDHs on the seawater evaporation performance of PB is examined. First, the equivalent amount of PB in every sample is confirmed by element analyzer (CHNS mode). Table 1 lists the amounts of N and corresponding PB. The data indicate that the amount of PB decreases with the increase of Mg/Al molar ratio, which determines the concentration of interlayer anions according to the literature.[27] Moreover, the SDS is employed as a dispersant to co-intercalated with PB. From Table 1, the amount of PB molecules reduces with the increase of SDS in the interlayer of LDHs.

To test seawater evaporation performance of powder samples, all the samples (50 mg of PB equivalent) were coated uniformly on the commercial polyurethane foam. When exposed to simulated sunlight (1 $kW \cdot m^{-2} \cdot h^{-1}$), the evaporation rates of seawater increase with the enhanced dispersion of PB as demonstrated in Fig. 5a-b: 0.39 $kg \cdot m^{-2} \cdot h^{-1}$ (Prussian blue), 0.43 $kg \cdot m^{-2} \cdot h^{-1}$ (PBA@LDHs-2), 0.45 $kg \cdot m^{-2} \cdot h^{-1}$ (PBA@LDHs-3), 0.49 $kg \cdot m^{-2} \cdot h^{-1}$ (PBA@LDHs-4), and 0.53 $kg \cdot m^{-2} \cdot h^{-1}$ (SDS-PBA_2@LDHs). However, excessively low concentrations of PB can disrupt the intermolecular charge transfer between Fe^{2+} and Fe^{3+}, mediated by cyanide bridges,[52, 53] resulting in decreased photothermal conversion performance and evaporation rate (0.47 $kg \cdot m^{-2} \cdot h^{-1}$ for SDS-PBA_1@LDHs). Moreover, the powders containing 20 mg of PB equivalent were mixed with high rebound compounds to form polyurethane mixtures. Thanks to the low density of the foamed composite material, it can float stably on the water (Fig. S2). Besides, the hydrophilicity was measured by the water contact angle and it

Table 1 Content of N and equivalent Prussian blue in LDHs.

Samples	N (%)	Prussian blue (%)	Structural formula
PBA@LDHs-2	7.29	25.69	$Mg_4Al_2Fe_{4/9}[Fe(CN)_6]_{2/3}(CO_3)_{4/9}(OH)_{12} \cdot 5.6H_2O$
PBA@LDHs-3	6.58	23.19	$Mg_6Al_2Fe_{4/9}[Fe(CN)_6]_{2/3}(CO_3)_{4/9}(OH)_{16} \cdot 3H_2O$
PBA@LDHs-4	5.97	21.04	$Mg_8Al_2Fe_{4/9}[Fe(CN)_6]_{2/3}(CO_3)_{4/9}(OH)_{20} \cdot 0.6H_2O$
SDS-PBA_2@LDHs	4.51	15.89	$Mg_8Al_2Fe_{8/21}[Fe(CN)_6]_{4/7}SDS_{2/7}(CO_3)_{8/21}(OH)_{20} \cdot 3.4H_2O$

SDS-PBA$_1$@LDHs	4.17	14.69	$Mg_8Al_2Fe_{1/3}[Fe(CN)_6]_{1/2}SDS_{1/2}(CO_3)_{1/3}(OH)_{20}\cdot 1.4H_2O$

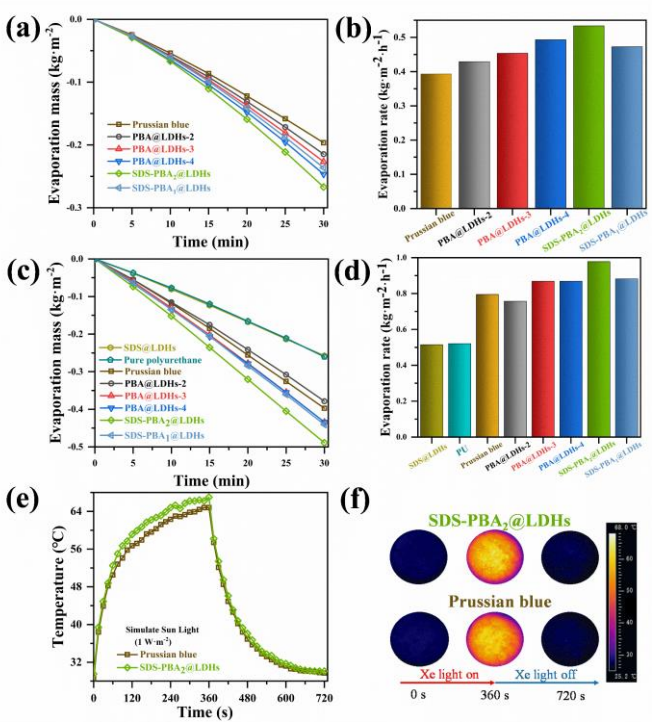

Fig. 5 (a) mass loss curves and (b) evaporation rate comparison of powders. (c) mass loss curves and (d) evaporation rate comparison of formed foams. (e) Photothermal conversion behavior of PB/PU and SDS-PBA$_2$@LDHs/PU under Xe light irradiation using AM1.5. (f) Time-sequence IR images of PB /PU and SDS-PBA$_2$@LDHs/PU.

was observed that the droplets were completely absorbed within about 2s (Fig. S3). In Fig. 5c-d, a significant improvement can be seen as compared to powders. It is attributed to the capability of 3D structure to recover the diffuse reflectance and reduce the thermal radiation heat loss compared to a 2D structure.[54] The highest evaporation rate of 0.98 kg·m^{-2}·h^{-1} is obtained from SDS-PBA$_2$@LDHs/PU, with a light-to-heat conversion efficiency of 66.3% (53.8% for PB/PU). To exclude the influence of SDS, the solar-water evaporation rates of SDS@LDHs/PU and pure PU are compared (Fig. 5d), revealing no obvious difference and remarkably lower than PBA@LDHs/PU. It is confirmed that SDS only acts as a dispersant for PBA in the interlayer. Inspired by the above-mentioned results, photothermal conversion behavior of PB/PU and SDS-PBA$_2$@LDHs/PU is tested under Xe light irradiation using an AM1.5 optical filter at power of 1 sun (1 kW·m^{-2}) (Fig. 5e-f). The temperature of SDS-PBA$_2$@LDHs/PU reaches 67°C in 6 min (64.8°C of PB/PU), indicating superior photothermal behavior. Table 2 summarizes the photothermal performance of different materials. SDS-PBA$_2$@LDHs achieves an average evaporation rate per milligram of effective substance of 0.049 kg·m^{-2}·h^{-1}·mg, which competes well with materials documented in other studies. Considering the cost-effectiveness, SDS-PBA$_2$@LDHs shows good competitiveness in the photothermal conversion domain.

Table 2 Comparison of photothermal performance of SDS-PBA$_2$@LDHs and other materials

Samples	Evaporation rate (kg·m^{-2}·h^{-1})	Optical concentration (kW·m^{-2})	evaporation rate/per milligram (kg·m^{-2}·h^{-1}·mg^{-1})	Ref.
CuO@PDA/PB	1.39	1	0.014	[56]
PB/PPy@CFs	1.36	1	0.008	[21]

AAO templates	0.67	1	——	[57]
Co_2C/PTFE	1.26	1	0.063	[58]
TiN	0.94	1	——	[59]
2D-$FeNi_3$/CNF-3	1.51	1	0.154	[60]
PU+CR-TPE-T	1.272	1	0.042	[61]
$Cu_{2-x}Se/Nb_2CT_X$	0.95	0.5	0.127	[62]
B@5/CNF	1.3	1	0.26	[63]
pDA-rGO/PTFE	0.72	1	——	[64]
rGO/MCE	0.838	1	0.042	[65]
CuS/PE	1.021	1	0.016	[66]
SDS-PBA_2@LDHs	0.98 ± 0.086	1	0.049	This work

Water stability analysis

To access the stability of SDS-PBA_2@LDHs, the dissolution loss of both insoluble PB[55] and SDS-PBA_2@LDHs is determined. Typically, 20 mg of each material are added into 50 mL of deionized water, stirred for 60 min, and then allowed to settle for 30 min. Moreover, the dissolution loss at different temperatures is tested, with the concentrations of Fe obtained by ICP-OES and detailed in Table 3. Interestingly, the dissolution rate of SDS-PBA_2@LDHs is 3 to 5 times lower than insoluble PB, that is, much lower than soluble PB (containing a monovalent metal ion inclusion complex that can dissociate into aqueous media).[28] At 65°C, the concentration of Fe in solution is measured to be below 10 mg/L. The solution of SDS-PBA_2@LDHs also appears clearer than insoluble PB (Fig. 6a-b). It

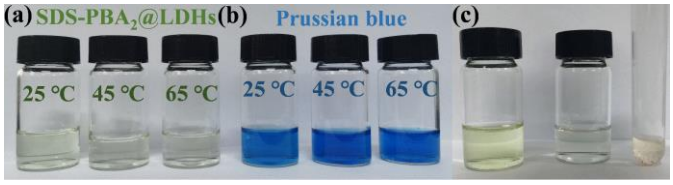

Fig. 6 The digital photos of (a)SDS-PBA_2@LDHs and (b) pristine PB in the aqueous solution at 25°C, 45°C, 65°C and (c) pH=10 at 25°C, supernatant of SDS-PBA_2@LDHs, supernatant of PB, and solution of PB (from left to right).

Table 3 Concentration of Fe dissolved from Prussian blue /SDS-PBA_2@LDHs.

	25℃	45℃	65℃	pH=10
	Concentration of Fe (mg/L)			
Prussian blue	16.99 ± 0.10	24.55 ± 0.03	23.08 ± 0.22	——
SDS-PBA_2@LDHs	6.23 ± 0.15	5.25 ± 0.16	4.10 ± 0.11	26.09 ± 0.35

is confirmed that PBA intercalated within LDHs has higher water stability than conventional PBAs. Further, the water stability ofSDS-PBA_2@LDHs is explored in alkaline environment at a pH of 10. It is worth noting that while PB decomposes and results in reddish-brown ferric hydroxide deposits (Fig. 6c), the SDS-PBA_2@LDHs remains clear. The Fe concentration dissolved from SDS-PBA_2@LDHs in alkaline solution is measured to be 26.09 mg/L, comparable to the one in neutral solution of PB. These results can be attributed to the immobilization of PB in the LDH galleries[50] and the protective effect of layers on the anions, which contributes to the reduced environmental impact of PB.

Conclusions

In summary, the intercalation of PB into LDHs has enhanced its photothermal conversion efficiency by preventing PB aggregation. The dispersion of PB can be finely regulated by altering the Mg/Al molar ratio within the layers and the concentration of SDS in the interlayers. The as-prepared powder sample exhibits a 35.9% increase in the rate of solar vapor generation compared to an equivalent amount of pristine PB (20 mg). The unique structure of LDHs has contributed to the enhanced thermal and water stability. Notably, due to the three-dimensional structure of high rebound foam, the solar water evaporation rate of the dispersed PB (20 mg) within the foam reaches 0.98 $kg \cdot m^{-2} \cdot h^{-1}$, surpassing pristine PB. The corresponding solar-to-water efficiency increases from 53.8% to 66.3%. To conclude, this intercalation method allows for the controlled adjustment of PB's dispersion, thus fine-tuning the photothermal performance using a straightforward synthesis approach. This work holds great potential for solar water evaporation.

Author Contributions

Conceptualization, W.M. H.L., and Y.F.; investigation and methodology, W.M., Q.H., and Y.J.; writing—original draft preparation, W.M.; writing—review and editing, J.G., W.T., F.L. and Y.F.; supervision, H.L. and Y.F. All authors have read and agreed to the published version of the manuscript.

Conflicts of interest

The authors declare that they have no known competing financial interests or personal relationships that could have appeared to influence the work reported in this paper.

Acknowledgements

This work is supported by Central Government Guiding Funds for Local Science and Technology Development (2022ZY015)，Nanjiang Technology Project （2023AB028), and Open Laboratory of State Key Laboratory of Organic and Inorganic Composites (oic-202301006).

References

1. J. H. Reif and W. Alhalabi, *Renewable and Sustainable Energy Reviews*, 2015, **48**, 152-165.
2. L. Zhu, M. Gao, C. K. N. Peh and G. W. Ho, *Nano Energy*, 2019, **57**, 507-518.
3. Y. Li, Y. Shi, H. Wang, T. Liu, X. Zheng, S. Gao and J. Lu, *Carbon Energy*, 2023, **5**, 331-372.
4. Q. Wen, L. Zhang, X. Fei and J. Li, *IOP Conference Series: Earth and Environmental Science*, 2019, **267**, 022030-022036.
5. M. Elimelech and W. A. Phillip, *Science*, 2011, **333**, 712-717.
6. F. Giacalone, P. Catrini, L. Gurreri, A. Tamburini, A. Cipollina, G. Micale and A. Piacentino, *Energy Conversion and Management*, 2022, **258**, 115314-115332.
7. A. J. Toth, *Membranes (Basel)*, 2020, **10**, 265-282.
8. R. Li, C. Zhou, L. Yang, J. Li, G. Zhang, J. Tian and W. Wu, *Journal of Hazardous Materials*, 2022, **424**, 127367-127379.
9. Z. Qin, Y. Li and N. Gu, *Advanced Healthcare Materials*, 2018, **7**, 1800347-1800359.
10. L. Doveri, A. Taglietti, P. Grisoli, P. Pallavicini and G. Dacarro, *Dalton Transactions*, 2023, **52**, 452-460.
11. W. J. Li, C. Han, G. Cheng, S. L. Chou, H. K. Liu and S. X. Dou, *Small*, 2019, **15**, 1900470-1900490.
12. Z.-Y. Yu, Y. Duan, J.-D. Liu, Y. Chen, X.-K. Liu, W. Liu, T. Ma, Y. Li, X.-S. Zheng, T. Yao, M.-R. Gao, J.-F. Zhu, B.-J. Ye and S.-H. Yu, *Nature Communications*, 2019, **10**, 2799-2807.
13. Z. Qin, B. Chen, X. Huang, Y. Mao, Y. Li, F. Yang and N. Gu, *Dalton Transactions*, 2019, **48**, 17169-17173.
14. Y. Xu, S. Zheng, H. Tang, X. Guo, H. Xue and H. Pang, *Energy Storage Materials*, 2017, **9**, 11-30.
15. A. A. Kadam, J. Jang and D. S. Lee, *Bioresource Technology*, 2016, **216**, 391-398.
16. X. Cai, W. Gao, M. Ma, M. Wu, L. Zhang, Y. Zheng, H. Chen and J. Shi, *Advanced Materials*, 2015, **27**, 6382-6389.
17. J. K. Zaręba, J. Szeremeta, M. Waszkielewicz, M. Nyk and M. Samoć, *Inorganic Chemistry*, 2016, **55**, 9501-9504.
18. J. Fu, B. Wu, M. Wei, Y. Huang, Y. Zhou, Q. Zhang and L. Du, *Acta Pharmaceutica Sinica B*, 2019, **9**, 604-614.
19. M. Gautam, K. Poudel, C. S. Yong and J. O. Kim, *International Journal of Pharmaceutics*, 2018, **549**, 31-49.
20. Q. Fang, G. Li, H. Lin and F. Liu, *Journal of Materials Chemistry A*, 2019, **7**, 8960-8966.
21. X. Wang, D. Yang, X. An and X. Qian, *Polymers (Basel)*, 2021, **14**, 14010006-14010020.
22. Y. Su, S. Qiu, D. Yang, S. Liu, H. Zhao, L. Wang and Q. Xue, *Journal of Hazardous Materials*, 2020, **391**, 122215-122229.
23. S. Iftekhar, V. Srivastava and M. Sillanpää, *Chemical Engineering Journal*, 2017, **309**, 130-139.
24. L. Jiang, J. Liu, K. Zuo, L. Zou, Y.-Y. Li, G. Qian and Z. P. Xu, *Bioresource Technology*, 2018, **259**, 99-103.
25. J. Yu, Q. Wang, D. O'Hare and L. Sun, *Chemical Society Reviews*, 2017, **46**, 5950-5974.
26. C. Taviot‐Guého, V. Prévot, C. Forano, G. Renaudin, C. Mousty and F. Leroux, *Advanced Functional Materials*, 2017, **28**, 1703868-1703900.
27. V. Rives and M. a. Angeles Ulibarri, *Coordination Chemistry Reviews*, 1999, **181**, 61-120.
28. S. Chen, X. Yang, Z. Wang, J. Hu, S. Han, Y. Guo and T. Deng, *Journal of Hazardous Materials*, 2021, **410**, 124608-124618.

29. Q. Wang, H. Wang, L. Yang, H. Yao, Z. Wu, T. Yu, K. Shi and S. Ma, *Journal of Materials Chemistry A*, 2022, **10**, 17520-17531.
30. P. Ma, Y. Hou, Z. Chen, J. Su, L. Li, N. Liu, Z. Zhang, X. Jiang, F. Long, Y. Ma and Y. Gao, *Chemical Engineering Journal*, 2021, **425**, 130471-130479.
31. X. Zhang, J. Lu, L. Jin and M. Wei, *Science Bulletin*, 2008, **53**, 1329-1336.
32. H. Zeng, L. Deng, Z. Shi, J. Luo and J. Crittenden, *Journal of Materials Chemistry A*, 2019, **7**, 342-352.
33. J. Wang, X. Wang, L. Tan, Y. Chen, T. Hayat, J. Hu, A. Alsaedi, B. Ahmad, W. Guo and X. Wang, *Chemical Engineering Journal*, 2016, **297**, 106-115.
34. C. Zhang, C. Yan, Z. Xue, W. Yu, Y. Xie and T. Wang, *Small*, 2016, **12**, 5320-5328.
35. L. Cui, P. Wang, H. Che, X. Gao, J. Chen, B. Liu and Y. Ao, *Applied Catalysis B: Environmental*, 2023, **330**, 122556-122566.
36. J. Zhu, X. Wang, J. Liang, X. Qiu, S. Chen, Y. Wang and Y. Wang, *EcoMat*, 2023, **5**, 12323-12333.
37. K. Cermelj, K. Ruengkajorn, J.-C. Buffet and D. O'Hare, *Journal of Energy Chemistry*, 2019, **35**, 88-94.
38. A. Pastor, F. Rodriguez-Rivas, G. d. Miguel, M. Cruz-Yusta, F. Martin, I. Pavlovic and L. Sánchez, *Chemical Engineering Journal*, 2020, **387**, 124110-124119.
39. M. Wilhelm, M. C. Quevedo, A. Sushkova, T. L. P. Galvão, A. Bastos, M. Ferreira and J. Tedim, *European Journal of Inorganic Chemistry*, 2020, **2020**, 2063-2073.
40. S. Zheng, J. Lu, J. Shi and X. Duan, *RSC Advances*, 2017, **7**, 2789-2795.
41. S. Lei, S. Wang, B. Gao, Y. Zhan, Q. Zhao, S. Jin, G. Song, X. Lyu, Y. Zhang and Y. Tang, *Journal of Colloid and Interface Science*, 2020, **577**, 181-190.
42. Y. Hu, S. Zhang, C. Luo, L. Wan, S. Wu, S. A. Baig and X. Xu, *Journal of Environmental Chemical Engineering*, 2022, **10**, 107776-107786.
43. L. Deng, H. Zeng, Z. Shi, W. Zhang and J. Luo, *Journal of Colloid and Interface Science*, 2018, **521**, 172-182.
44. R. Amini, E. Rahimpour and A. Jouyban, *Analytica Chimica Acta*, 2020, **1117**, 9-17.
45. H. S. Panda, R. Srivastava and D. Bahadur, *The Journal of Physical Chemistry C*, 2009, **113**, 9560-9567.
46. J. Gao, Z. Xing, J. Zhou, H. Xu, Z. Wang, G. Li and L. Yu, *Dalton Transactions*, 2022, **51**, 5127-5137.
47. Y. Wu, H. Huang, W. Zhou, C. You, H. Ye, J. Chen, S. Zang, J. Yun, X. Chen, L. Wang and Z. Yuan, *ACS Applied Materials & Interfaces*, 2022, **14**, 29099-29110.
48. D. Parajuli, H. Tanaka, K. Sakurai, Y. Hakuta and T. Kawamoto, *Materials*, 2021, **14**, 1151-1167.
49. N. Tang, T. He, J. Liu, L. Li, H. Shi, W. Cen and Z. Ye, *Nanoscale Research Letters*, 2018, **13**, 1-7.
50. G. Mishra, B. Dash and S. Pandey, *Applied Clay Science*, 2018, **153**, 172-186.
51. J. Wang, L. Zhao, H. Shi and J. He, *Angewandte Chemie International Edition*, 2011, **50**, 9171-9176.
52. W. Zhu, K. Liu, X. Sun, X. Wang, Y. Li, L. Cheng and Z. Liu, *ACS Applied Materials & Interfaces*, 2015, **7**, 11575-11582.
53. M. F. Dumont, H. A. Hoffman, P. R. S. Yoon, L. S. Conklin, S. R. Saha, J. Paglione, R. W. Sze and R. Fernandes, *Bioconjugate Chemistry*, 2013, **25**, 129-137.
54. Y. Shi, R. Li, Y. Jin, S. Zhuo, L. Shi, J. Chang, S. Hong, K.-C. Ng and P. Wang, *Joule*, 2018, **2**, 1171-1186.
55. G. Dacarro, A. Taglietti and P. Pallavicini, *Molecules*, 2018, **23**, 1414-1433.
56. R. Zhu, M. Liu, Y. Hou, D. Wang, L. Zhang, D. Wang and S. Fu, *Chemical Engineering Journal*, 2021, **423**, 129099-129111.
57. K. Bae, G. Kang, S. K. Cho, W. Park, K. Kim and W. J. Padilla, *Nature Communications*, 2015, **6**, 10103-10111.
58. Z. Yang, T. Zhao, S. Hao, R. Wang, C. Zhu, Y. Tang, C. Guo, J. Liu, X. Wen and F. Wang, *Advanced Science*, 2023, **10**, 2301073-2301082.
59. Y. Zhang, K. Li, L. Liu, K. Wang, J. Xiang, D. Hou and J. Wang, *Chemosphere*, 2020, **256**, 127053-127061.
60. H. Li, M. Aizudin, S. Yang, Z. Guo, J. Yang, F. Yang, E. Huixiang Ang and J. Pan, *Separation and Purification Technology*, 2023, **326**, 124802-124812.
61. G. Chen, J. Sun, Q. Peng, Q. Sun, G. Wang, Y. Cai, X. Gu, Z. Shuai and B. Z. Tang, *Advanced Materials*, 2020, **32**, 1908537-1908545.
62. W. Xia, H. Cheng, S. Zhou, N. Yu and H. Hu, *Journal of Colloid and Interface Science*, 2022, **625**, 289-296.
63. X. Guan, P. Kumar, Z. Li, T. K. A. Tran, S. Chahal, Z. Lei, C. Y. Huang, C. H. Lin, J. K. Huang, L. Hu, Y. C. Chang, L. Wang, J. S. J. Britto, L. Panneerselvan, D. Chu, T. Wu, A. Karakoti, J. Yi and A. Vinu, *Advanced Science*, 2023, **10**, 2205809-2205818.
64. L. Huang, J. Pei, H. Jiang and X. Hu, *Desalination*, 2018, **442**, 1-7.
65. G. Wang, Y. Fu, X. Ma, W. Pi, D. Liu and X. Wang, *Carbon*, 2017, **114**, 117-124.
66. M. Shang, N. Li, S. Zhang, T. Zhao, C. Zhang, C. Liu, H. Li and Z. Wang, *ACS Applied Energy Materials*, 2017, **1**, 56-61.